

pubs.acs.org/JACS Article

# How the Bioinspired Fe<sub>2</sub>Mo<sub>6</sub>S<sub>8</sub> Chevrel Breaks Electrocatalytic **Nitrogen Reduction Scaling Relations**

Nicholas R. Singstock and Charles B. Musgrave\*



Cite This: J. Am. Chem. Soc. 2022, 144, 12800-12806



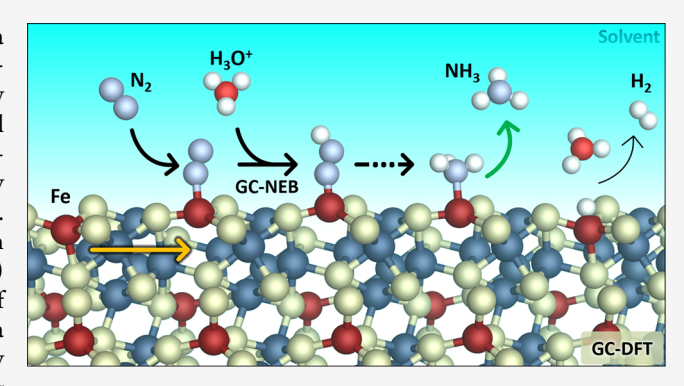
ACCESS I

Metrics & More

Article Recommendations

Supporting Information

ABSTRACT: The nitrogen reduction reaction (NRR) is a renewable alternative to the energy- and CO2-intensive Haber-Bosch NH3 synthesis process but is severely limited by the low activity and selectivity of studied electrocatalysts. The Chevrel phase Fe<sub>2</sub>Mo<sub>6</sub>S<sub>8</sub> has a surface Fe-S-Mo coordination environment that mimics the nitrogenase FeMo-cofactor and was recently shown to provide state-of-the-art activity and selectivity for NRR. Here, we elucidate the previously unknown NRR mechanism on Fe<sub>2</sub>Mo<sub>6</sub>S<sub>8</sub> via grand-canonical density functional theory (GC-DFT) that realistically models solvated and biased surfaces. Fe sites of Fe<sub>2</sub>Mo<sub>6</sub>S<sub>8</sub> selectively stabilize the key \*NNH intermediate via a narrow band of free-atom-like surface d-states that selectively hybridize with p-states of \*NNH, which results in Fe sites breaking



NRR scaling relationships. These sharp d-states arise from an Fe-S bond dissociation during N2 adsorption that mimics the mechanism of the nitrogenase FeMo-cofactor. Furthermore, we developed a new GC-DFT-based approach for calculating transition states as a function of bias (GC-NEB) and applied it to produce a microkinetic model for NRR at Fe<sub>2</sub>Mo<sub>6</sub>S<sub>8</sub> that predicts high activity and selectivity, in close agreement with experiments. Our results suggest new design principles that may identify effective NRR electrocatalysts that minimize the barriers for \*N<sub>2</sub> protonation and \*NH<sub>3</sub> desorption and that may be broadly applied to the rational discovery of stable, multinary electrocatalysts for other reactions where narrow bands of surface d-states can be tuned to selectively stabilize key reaction intermediates and guide selectivity toward a target product. Furthermore, our results highlight the importance of using GC-DFT and GC-NEB to accurately model electrocatalytic reactions.

# INTRODUCTION

The synthesis of ammonia from nitrogen is a foundation of modern society due to the critical role it plays in producing ammonia for fertilizers that support feeding nearly half of the global population.<sup>1,2</sup> Over 90% of the world's 235 Mt/year production of NH3 is generated via the Haber-Bosch process, which is highly energy intensive and generates ~1.8% of global CO<sub>2</sub> emissions annually.<sup>3-9</sup> Synthesis of NH<sub>3</sub> via the electrocatalytic nitrogen reduction reaction (NRR) is a promising alternative process because it can be powered by renewable electricity, uses N2 and H2O as sustainable inputs, and enables distributed production. 4,7,8,10,11 Ammonia produced by NRR is also a promising fuel for renewable energy storage and a renewable precursor to other industrial chemicals such as nitric acid.<sup>2,12</sup> Yet, the development of NRR has been limited by the absence of an active and selective electrocatalyst, with the majority of currently studied materials yielding Faradaic efficiencies (FE) of <1% due to competition with proton reduction via the hydrogen evolution reaction (HER). 4,6,7,13-20 This results from linear scaling relationships between NRR intermediates that limit NRR activity, where previous work indicated that metals with weaker nitrogen binding are limited by the reductive adsorption of  $N_2$  to form

\*NNH and metals with stronger binding are limited by the reductive desorption of \*NH2 to form NH3 (\* denotes adsorbed species).4,21

In nature, NH3 is synthesized from N2 by nitrogenase enzymes in conjunction with a catalytic FeMo-cofactor. 22-24 The impressive activity of the cofactor is enabled by its structure, which is comprised of Fe active sites coupled with Mo through sulfur atoms (Figure 1a). An analogous inorganic structure is the metallic Chevrel phase Fe<sub>2</sub>Mo<sub>6</sub>S<sub>8</sub>, where Fe atoms coordinate to Mo<sub>6</sub> octahedra through sulfur atoms (Figure 1b). The Fe-S-Mo coordination environment of the predominant (101) surface of the PI Fe<sub>2</sub>Mo<sub>6</sub>S<sub>8</sub> crystal structure closely resembles that of the Fe active site of the FeMo-cofactor and may therefore also provide favorable energetics for ambient conversion of N<sub>2</sub> to NH<sub>3</sub>. Furthermore,

Received: April 5, 2022 Published: July 11, 2022





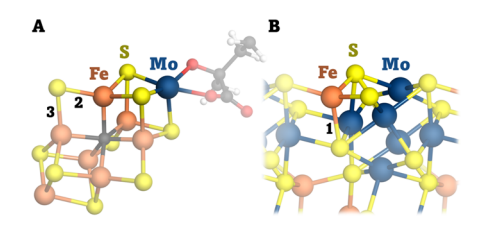


**Figure 1.** Structural similarities of Fe–S–Mo bonding. Ground-state structures of the nitrogenase FeMo-cofactor (A) and (101)  $\text{Fe}_2\text{Mo}_6S_8$  Chevrel phase surface (B). The similar Fe–S–Mo coordination of the structures is highlighted.

during the preparation of this report, an experimental investigation of Fe<sub>2</sub>Mo<sub>6</sub>S<sub>8</sub>-catalyzed NRR found that it yielded a state-of-the-art FE of 12.5% and a high rate of 70  $\mu$ g NH<sub>3</sub> h<sup>-1</sup> mg<sub>cat</sub><sup>-1</sup> at a low bias of -0.20 V vs RHE, which was stable over 50 h.<sup>25</sup> However, the mechanism for NRR on this impressive material has not yet been determined, limiting the understanding necessary to rationally design superior electrocatalysts in this material space. <sup>26,27</sup>

To probe the NRR reaction mechanism on Fe<sub>2</sub>Mo<sub>6</sub>S<sub>8</sub> under realistic reaction conditions, that is, in solvent under an applied bias, we used grand-canonical density functional theory (GC-DFT, see Section S1 for details)<sup>28-30</sup> and implemented a new GC-DFT approach to calculate reaction barriers as a function of the applied bias (GC-NEB, see Computational Details). GC-NEB predicts low barriers for both \*N2 protonation to \*NNH and \*NH3 desorption, which we identified to be the two key steps that limit NRR on this material. Consequently, we find that Fe surface sites on Fe<sub>2</sub>Mo<sub>6</sub>S<sub>8</sub> facilitate rapid NRR rates (>6  $\mu$ g h<sup>-1</sup> cm<sup>-2</sup>) due to the selective stabilization of the key \*NNH intermediate relative to \*N2. N2 adsorption at Fe sites results in a concomitant dissociation of the subsurface Fe-S bond (1 in Figure 1), similar to the  $N_2$  reduction mechanism on the nitrogenase FeMo- and FeV-cofactors where two Fe–S bonds dissociate (2 and 3 in Figure 1) to reveal the Fe active sites.  $^{17,22,31}$  On Fe<sub>2</sub>Mo<sub>6</sub>S<sub>8</sub>, this yields a Fe active site with narrow bands of free-atom-like d-states that overlap significantly with the nitrogen p-states of \*NNH but not those of \*N2 or \*NH3, which selectively stabilizes \*NNH to break linear NRR scaling relationships. The elucidation of the NRR mechanism on Fe<sub>2</sub>Mo<sub>6</sub>S<sub>8</sub> provides important insights

that may aid in the rational design of superior electrocatalysts with high  $NH_3$  activity and selectivity.

## RESULTS AND DISCUSSION

NRR Mechanism on Fe<sub>2</sub>Mo<sub>6</sub>S<sub>8</sub>. NRR involves the transfer of six protons and six electrons to N2 to yield two NH3 molecules. In electrocatalytic NRR, the protons and electrons are derived from an anodic oxidation (e.g., oxygen evolution reaction) and are transferred to the \*N<sub>x</sub>H<sub>y</sub> species from the solvent and NRR electrocatalyst, respectively. Three reaction mechanisms have been proposed for NRR: (1) the associative alternating pathway, where the nitrogen atoms of \*N2 are protonated in parallel to form \*NH2NH2 and then \*NH3 (Figure 2, opaque), (2) the associative distal pathway, where the nitrogen atoms are protonated in series to form \*NNH<sub>3</sub> and then \*NH3 (Figure 2, transparent), and (3) the dissociative pathway, where N2 dissociatively adsorbs into two \*N atoms at separate sites, which are subsequently protonated. 4,17,18 The dissociative pathway is not considered further due to its large change in grand free energy  $(\Delta\Phi)$  on  $Fe_2Mo_6S_8$ , which ranges from 2.81 to 2.44 eV at 0.0 V and -0.5 V, respectively (see Figure S1). In addition to these three NRR mechanisms, we also examined a hydride-based mechanism, analogous to the Lowe-Thorneley mechanism of biological N2 reduction by the FeMo-cofactor of nitrogenase (Section S2); 17,32 however, we found that this mechanism has a negligible contribution to NRR on Fe<sub>2</sub>Mo<sub>6</sub>S<sub>8</sub>.

Chevrel phase Fe<sub>2</sub>Mo<sub>6</sub>S<sub>8</sub> is a multisite catalyst with Mo, Fe, and S surface sites that bind nitrogen and hydrogen. Here, we consider the (101) surface of the triclinic  $P\overline{1}$  Fe<sub>2</sub>Mo<sub>6</sub>S<sub>8</sub> crystal structure (Table S1-1), which we previously showed by powder X-ray diffraction to be the predominant surface and crystal structure of Fe<sub>2</sub>Mo<sub>6</sub>S<sub>8</sub> at ambient conditions.<sup>33</sup> Figure 2a,b shows the GC-DFT-computed energies for the associative NRR pathways on Mo and Fe surface sites, respectively, in  $H_2O$  solvent and under an applied bias of 0.0 to -0.5 V, which spans the range of commonly studied reducing biases. 6,15,25 Nitrogen and hydrogen binding is not favorable at S sites (Figure S2), while at Mo sites, NRR proceeds via either the associative alternating or associative distal pathways (Figure 2a). However, the final reaction step of both pathways is \*NH<sub>3</sub> desorption, which requires a large grand free energy  $(\Delta\Phi_2)$  of 1.16-1.32 eV at the considered biases. Consequently, the rate

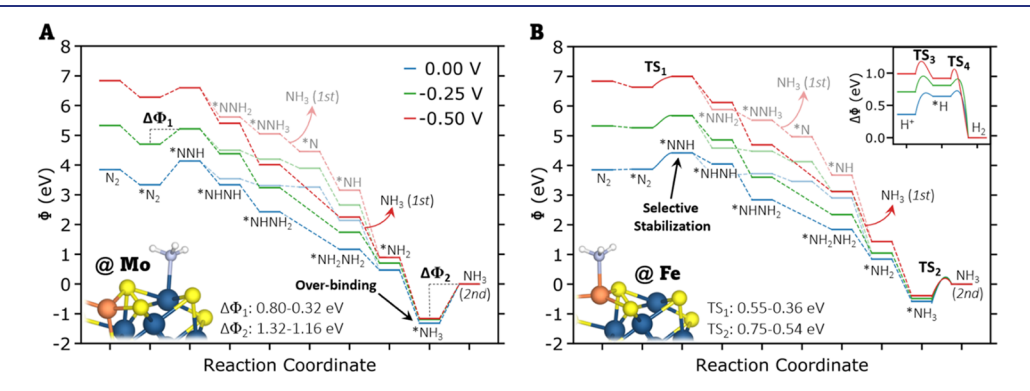


Figure 2. NRR Mechanism on  $Fe_2Mo_6S_8$ . The associative alternating (opaque) and associative distal (transparent) NRR pathways at Mo (A) and Fe (B) surface sites, at applied biases of 0.0, -0.25, and -0.5 V vs RHE (red, green, and blue, respectively) in  $H_2O$  solvent at pH 7. The Volmer–Heyrovsky HER pathway on Fe sites is shown in the inset. Transition states are included for  $*N_2$  protonation (TS<sub>1</sub>),  $*NH_3$  desorption (TS<sub>2</sub>),  $H^+$  adsorption (TS<sub>3</sub>), and \*H protonation (TS<sub>4</sub>) on Fe sites. NH<sub>3</sub>(aq) is set as the grand free energy (Φ) reference, which results in the bias dependence of the initial state. The energies for each pathway and bias are provided in Table S1.

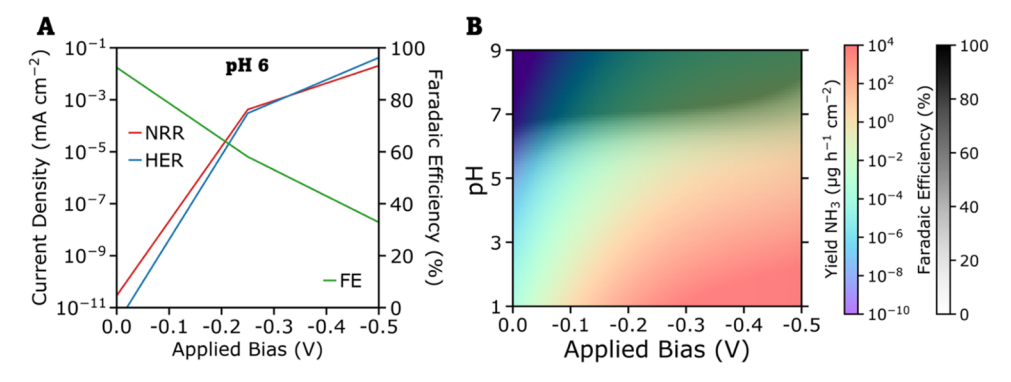


Figure 3. NRR microkinetic model. Current densities for NRR and HER, and NRR Faradaic efficiency (A) were calculated at biases of 0.0, -0.25, and -0.5 V at pH 6 using an NRR microkinetic model based on reaction barriers computed by GC-NEB. (B) Heatmap of NH<sub>3</sub> yield (color) and NRR FE (black & white shading) as pH and applied bias are varied in the NRR microkinetic model for Fe<sub>2</sub>Mo<sub>6</sub>S<sub>8</sub>. Both Fe and Mo sites are considered in the microkinetic model.

of NH<sub>3</sub> production  $(r_{\rm NH_3})$  from Mo sites between 0.0 and -0.5 V is negligibly low, with  $r_{\rm NH_3} < 4.4 \times 10^{-5}~\mu \rm g~NH_3~h^{-1}~cm^{-2}$  (i.e.,  $4.2 \times 10^{-7}~\rm mA~cm^{-2}$ ) and a \*NH<sub>3</sub> coverage > 99.999% if no additional activation barriers exist that would further lower NRR activity (i.e.,  $TS_2 \ge \Delta \Phi_2$ ). Consequently, our calculations predict that Mo sites are poisoned by over-binding of \*NH<sub>3</sub>, which results in negligible NRR and HER activity at these sites at biases between 0.0 and -0.5 V (Figure S3).

NRR at Fe sites may also proceed through either associative pathway (Figure 2b), which both involve the same key reaction steps: \*N $_2$  protonation to form \*NNH and \*NH $_3$  desorption. Relative to binding at Mo sites,  $N_2$  and NH $_3$  binding energies are shifted by +0.53 and +0.66 eV at 0 V, respectively. This suggests that Fe sites bind NRR intermediates more weakly than Mo sites. However, the binding energy of \*NNH is -0.03 eV lower on Fe sites than on Mo sites, indicating that Fe sites selectively stabilize the \*NNH intermediate relative to \*N $_2$ , which lowers the grand free energy of \*N $_2$  protonation ( $\Delta\Phi_1$ ). Consequently,  $\Delta\Phi_1$  and  $\Delta\Phi_2$  are both lower on Fe sites than on Mo sites. The  $\Delta\Phi$  for these steps on Fe sites is not affected by \*NH $_3$  adsorption at neighboring Mo sites (Figure S4). The selective stabilization of \*NNH on Fe surface sites results in Fe $_2Mo_6S_8$  favorably breaking linear NRR scaling relationships.

Grand Canonical Microkinetic Modeling. To compute the kinetics of Fe<sub>2</sub>Mo<sub>6</sub>S<sub>8</sub>-catalyzed NRR, we developed and applied a grand canonical implementation of the nudged elastic band method (GC-NEB, see Computational Details) to calculate the activation energies  $(\Phi_a)$  for four key transition states (TSs) on Fe sites: (1)  $N_2$  protonation by  $H_3O^+$  to form \*NNH and H<sub>2</sub>O (TS<sub>1</sub>), (2) \*NH<sub>3</sub> desorption (TS<sub>2</sub>), (3) proton adsorption from H<sub>3</sub>O<sup>+</sup> to form H\* and H<sub>2</sub>O (HER, Volmer step, TS<sub>3</sub>), and (4) H\* protonation by H<sub>3</sub>O<sup>+</sup> to form H<sub>2</sub> and H<sub>2</sub>O (HER, Heyrovsky step, TS<sub>4</sub>). The TS grand free energies are shown in Figure 2b as a function of bias. TS<sub>1</sub> has a low  $\Phi_a$  at all three biases, decreasing from 0.55 to 0.36 eV as the bias decreases from 0.0 to -0.5 V, resulting in a large rate constant (k) of >1.9  $\times$  10<sup>4</sup> M<sup>-1</sup> s<sup>-1</sup>. \*NH<sub>3</sub> desorbs reductively, requiring ~0.40 electrons to be transferred to the desorbing NH<sub>3</sub>. Consequently, TS<sub>2</sub> is bias-dependent, with a  $\Phi_a$  that decreases from 0.75 eV at 0.0 V to 0.54 eV at -0.5 V. This results in an increase in k from 8.1 to  $2.9 \times 10^4$  s<sup>-1</sup>. Thus, NRR at the Fe sites of Fe<sub>2</sub>Mo<sub>6</sub>S<sub>8</sub> proceeds via low  $\Phi_a$ s for both TS<sub>1</sub> and TS2 due to the selective stabilization of \*NNH and the moderate binding energy of \*NH<sub>3</sub>. The RDS between 0.0 and -0.5 V is TS<sub>2</sub>. Non-GC approaches, such as the computational

hydrogen electrode (CHE), fail to capture the bias dependence of the RDS because it is not a proton-coupled electron transfer. GC-NEB was also used to compute the  $\Phi_a s$  of the Volmer–Heyrovsky mechanism for HER at Fe sites to determine the activity of this reaction and the resultant selectivity toward NRR. At 0.0 V, both the Volmer (H<sup>+</sup>  $\rightarrow$  H\*) and Heyrovsky (H<sup>+</sup> + H\*  $\rightarrow$  H<sub>2</sub>) steps have low  $\Phi_a s$  of 0.34 and 0.09 eV, respectively, with the Volmer step being rate limiting. At more reducing biases, the Volmer barrier decreases and the Heyrovsky barrier slightly increases, shifting to 0.23 and 0.11 eV, respectively, at -0.5 V.

We developed a microkinetic model for NRR and HER on  $Fe_2Mo_6S_8$  using the computed thermodynamics and  $\Phi_a$ s of each reaction step (see Section S3). Mo sites have a negligible contribution to the current densities of NRR and HER (Figure S3). The low  $\Phi_a$ s for both \*N<sub>2</sub> protonation and \*NH<sub>3</sub> desorption at Fe sites result in high selectivity toward NRR, with a FE of 81-99% at pH 7 and 33-92% at pH 6 (Figure 3a). However, at pH 6-7, the activity of NRR is low due to the low [H<sup>+</sup>], with a current density of  $2.1 \times 10^{-2}$  to  $2.1 \times 10^{-3}$ mA cm<sup>-2</sup>, respectively, at -0.5 V. Decreasing the solvent pH increases NRR activity; however, it also increases HER activity at a greater rate, resulting in a decrease of FE as pH decreases. This effect is evident in Figure 3b, where the NH<sub>3</sub> yield is maximized at lower pH and more reducing biases, but the FE is maximized at higher pH and less reducing biases. Figure 3b further demonstrates the challenge of identifying superior NRR electrocatalysts with desirable metrics for both activity and selectivity, which are maximized under different conditions. Despite this limitation, a pH of 5.5 combined with a bias of -0.5 V balances a high FE (17%) and a high NH<sub>3</sub> yield (6.9  $\mu$ g h<sup>-1</sup> cm<sup>-2</sup>), which is superior to most NRR electrocatalysts studied to date. 6,11,13 These results are in close agreement with recent experimental metrics of 12.5% FE and 3.9 μg NH<sub>3</sub> h<sup>-1</sup> cm<sup>-2</sup> at pH 4.5 and -0.2 V.<sup>25</sup> Our model predicts 14.6% FE and  $1.8 \times 10^{-2} \,\mu g \, \text{NH}_3 \, \text{h}^{-1} \, \text{cm}^{-2}$  at pH 4.5 and  $-0.2 \, \text{V}$ , despite the exponential sensitivity of NRR activity and selectivity on reaction conditions. The difference between the calculated and experimental activity values indicates an absolute error of only  $0.\overline{14}$  eV for the RDS  $\Phi_{av}$  highlighting the accuracy of GC-NEB to reproduce macroscopic NRR metrics and validating the proposed NRR mechanism and calculated energetics for Fe<sub>2</sub>Mo<sub>6</sub>S<sub>8</sub>.

We also developed a simplified microkinetic model based on energies calculated with the CHE approximation<sup>29</sup> (Figure

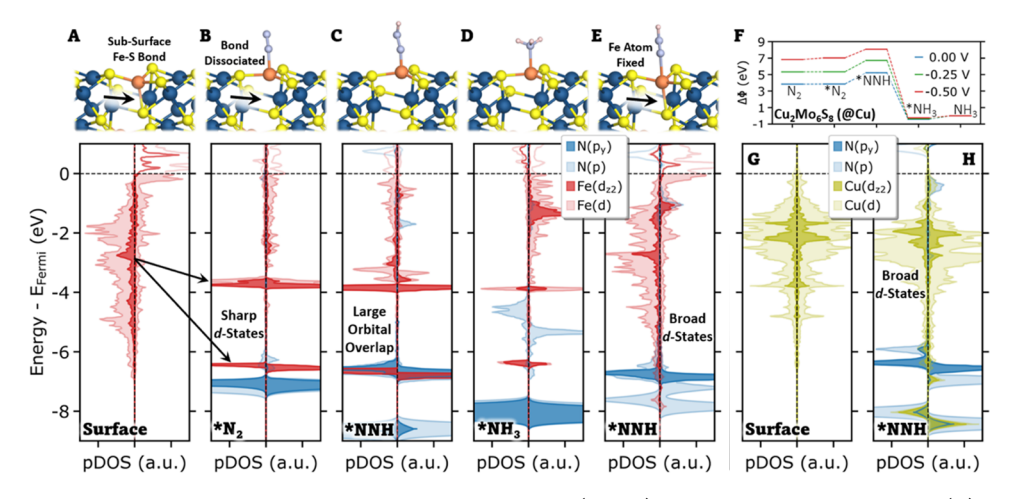


Figure 4. Selective \*NNH stabilization. Structure and projected density of states (pDOS) for the clean  $Fe_2Mo_6S_8$  surface (A), the  $Fe_2Mo_6S_8$  surface with \*N<sub>2</sub> (B), \*NNH (C), \*NH<sub>3</sub> (D), and \*NNH with the Fe surface atom fixed at its position on the clean surface (E). The abbreviated NRR mechanism on  $Cu_2Mo_6S_8$  (F) is included for comparison alongside the pDOS of the clean (G) and \*NNH covered (H)  $Cu_2Mo_6S_8$  surfaces. The pDOS for these structures is shown for the surface Fe/Cu atom and adsorbed \*N atom at 0.0 V.

S5), which deviates considerably from experiment (i.e., 1.8% FE and  $6 \times 10^{-4} \ \mu g \ NH_3 \ h^{-1} \ cm^{-2}$  at pH 4.5 and -0.20 V) and underscores the need for GC-DFT and GC-NEB to accurately model electrochemical NRR.

How Fe Sites Break Linear Scaling. The impressive activity and selectivity of the Fe surface sites of Fe<sub>2</sub>Mo<sub>6</sub>S<sub>8</sub> are a consequence of their selective stabilization of \*NNH relative to \*N<sub>2</sub> and \*NH<sub>3</sub>. This is consistent with the reactivity of the biological FeMo-cofactor, where Fe has been demonstrated as the active site for nitrogen reduction.<sup>17</sup> During N<sub>2</sub> adsorption on Fe sites of Fe<sub>2</sub>Mo<sub>6</sub>S<sub>8</sub>, a concurrent dissociation of the subsurface Fe-S bond occurs to stabilize the Fe-N bond (see Figure 4a,b), enabling an S<sub>N</sub>2 reaction for this step to activate the N<sub>2</sub> triple bond. This is similar to the N<sub>2</sub> reduction mechanism of the nitrogenase FeMo- and FeV-cofactors where two Fe-S bonds (2 and 3 in Figure 1) dissociate to produce the trigonal pyramidal Fe active sites. 17,22,31 Fe-S subsurface bond dissociation on Fe<sub>2</sub>Mo<sub>6</sub>S<sub>8</sub> also yields a trigonal pyramidal active site (tetrahedral with \*N<sub>x</sub>H<sub>y</sub>). This mechanism supports the biomimetic properties of Fe<sub>2</sub>Mo<sub>6</sub>S<sub>8</sub>. The Fe-S subsurface bond remains broken until \*NH3 desorbs (Figure 4d), whereas it remains intact upon proton adsorption at Fe sites.

An intriguing consequence of the subsurface Fe-S bond dissociation and the reorganization of the Fe site geometry is the narrowing of the  $d_z^2$  band of the surface Fe atom into freeatom-like states at -6.5 and -3.8 eV below the Fermi level. Narrow *d*-state bands in single-atom catalysts have been shown to influence selectivity via hybridization with the molecular orbitals of adsorbing molecules of a similar energy, which selectively stabilizes the adsorbates.<sup>34</sup> The bonding  $d_z^2$  state at -6.5 eV exhibits significant overlap with the  $p_y$  state of the bound N of \*NNH (Figure 4c); however, minimal overlap exists between these states in \*N2 and \*NH3 (Figure 4b,d). The large and selective overlap between the Fe  $d_z^2$  and \*NNH  $p_{\nu}$  states indicates a selective stabilization of \*NNH relative to \*N<sub>2</sub> or \*NH<sub>3</sub>, consistent with the calculated binding energies of these adsorbates. Additionally, we fixed the Fe surface atom in our model to its position on the clean surface and then adsorbed \*N2, \*NNH, and \*NH3 to the fixed Fe atom to determine the importance of the Fe-S bond dissociation on the binding energies of these adsorbates. This prevents the Fe-S bond from dissociating and the band of surface d-states

from narrowing (Figure 4e). Consequently, no selective stabilization of \*NNH is calculated when the Fe surface atom is fixed, and the  $\Delta\Phi$  for \*N<sub>2</sub> protonation to \*NNH is 1.19 eV at -0.5 V, vs 0.36 eV when the surface Fe atom is free to dissociate from the subsurface S atom. The Mo surface sites of Fe<sub>2</sub>Mo<sub>6</sub>S<sub>8</sub> possess a broad band of surface *d*-states that overlap similarly with the nitrogen *p*-states of \*N<sub>2</sub>, \*NNH, and \*NH<sub>3</sub> (Figure S6), which thus results in no selective stabilization of \*NNH (Figure 2a). Sharp nitrogen *p*-states exist at approximately -6.5 eV below the Fermi level for \*NNH at both Fe and Mo sites (Figure S6).

In contrast to Fe<sub>2</sub>Mo<sub>6</sub>S<sub>8</sub>, the measured FE and activity of NRR catalyzed by the Cu<sub>2</sub>Mo<sub>6</sub>S<sub>8</sub> Chevrel phase are an order of magnitude lower than that of Fe<sub>2</sub>Mo<sub>6</sub>S<sub>8</sub>, despite its similar structure, composition, and bulk electronic properties. 33,35 The Cu surface sites of the predominant (101) Cu<sub>2</sub>Mo<sub>6</sub>S<sub>8</sub> surface (see ref 33) bind more weakly to \*N2 and \*NH3 (see Figure 4f) and do not selectively stabilize \*NNH. This significantly increases the  $\Delta\Phi$  of \*N<sub>2</sub> protonation to 1.06–1.36 eV between 0.0 and -0.5 V vs 0.36-0.55 eV on Fe<sub>2</sub>Mo<sub>6</sub>S<sub>8</sub>, which dramatically decreases the calculated NRR activity of Cu sites to  $<1.0 \times 10^{-8} \mu g h^{-1} cm^{-2}$  at all conditions (Figure S7). Analogous to Fe<sub>2</sub>Mo<sub>6</sub>S<sub>8</sub>, \*NNH binding at Cu surface sites of Cu<sub>2</sub>Mo<sub>6</sub>S<sub>8</sub> causes a concomitant dissociation of the subsurface Cu-S bond. However, the Cu atom only shifts 0.54 Å in the zdirection vs a 0.76 Å shift of Fe in Fe<sub>2</sub>Mo<sub>6</sub>S<sub>8</sub>. Furthermore, the band of  $d_z^2$  states of the surface Cu atom does not narrow, and this broad band of d-states overlaps minimally with the N  $p_{\nu}$ states of \*NNH (Figure 4g,h). Thus, the negligible overlap of surface Cu  $d_z^2$  states with the \*NNH  $p_y$  states at Cu sites produces conventional scaling limitations of NRR intermediates on Cu<sub>2</sub>Mo<sub>6</sub>S<sub>8</sub> and ultimately low NRR activity and selectivity (Figure S7).

Our results demonstrate that superior NRR activity and selectivity may be achieved by materials that selectively stabilize \*NNH relative to \*N<sub>2</sub> and bind \*NH<sub>3</sub> weakly (e.g., Fe<sub>2</sub>Mo<sub>6</sub>S<sub>8</sub>). This suggests that new materials may be rapidly screened by their  $\Delta\Phi$  for \*N<sub>2</sub> protonation and \*NH<sub>3</sub> desorption to identify promising candidates that minimize the  $\Phi_{\rm a}$  barriers of both of these key reaction steps. We note that these proposed NRR screening criteria differ from the previously suggested NRR scaling relations of N<sub>2</sub>  $\rightarrow$  \*NNH vs

\*NH<sub>2</sub>  $\rightarrow$  NH<sub>3</sub>. <sup>21</sup> The multinary Chevrel phases may provide an ideal platform for designing superior NRR electrocatalysts due to the similarity of their active sites to the nitrogenase cofactors and their tunable compositions that allow a range of chalcogenide stoichiometries and transition-metal intercalants. <sup>36–38</sup> Expanding the set of NRR electrocatalysts that break scaling relations via GC-DFT studies may elucidate the importance of narrow bands of surface d-states near -6.5 eV below the Fermi level, concomitant N<sub>2</sub> adsorption and subsurface bond dissociation, and the trigonal pyramidal active site geometry (tetrahedral with \*N<sub>x</sub>H<sub>v</sub>).

# CONCLUSIONS

Fe<sub>2</sub>Mo<sub>6</sub>S<sub>8</sub> achieves state-of-the-art activity and selectivity for NRR via the selective stabilization of \*NNH relative to \*N<sub>2</sub> that results in low  $\Phi_a$ s for the key NRR reaction steps of \*N<sub>2</sub> protonation and \*NH<sub>3</sub> desorption. This selective stabilization results from the narrow band of free-atom-like *d*-states that arise via a biomimetic Fe–S bond dissociation during NRR. This suggests that a rational electrocatalyst design platform may be developed by compositionally tuning the Chevrel phases and that new materials may also be screened by their  $\Delta\Phi$ s of \*N<sub>2</sub> protonation and \*NH<sub>3</sub> desorption to identify promising NRR electrocatalysts that break scaling relations, analogous to Fe<sub>2</sub>Mo<sub>6</sub>S<sub>8</sub>.

Our results also highlight the need for a grand canonical approach for modeling electrocatalytic systems, which was necessary to illuminate the bias dependence of the RDS at Fe surface sites and to accurately predict NRR activity and selectivity. We anticipate that grand canonical modeling, including GC-NEB, will enable the development of realistic and accurate mechanisms and microkinetic models for other electrochemical reactions. Furthermore, the mechanism discovered here provides new insights that may guide the design of stable, multinary electrocatalysts for other reactions, where the energy levels of narrow bands of surface d-states may be tuned to selectively hybridize with key reaction intermediates, resulting in improved activity and/or selectivity toward a target product.

## COMPUTATIONAL DETAILS

**GC-DFT.** GC-DFT calculations were performed using the JDFTx software.  $^{39,40}$  All calculations were performed using the PBE functional,  $^{41}$  with the D2 van der Waals correction. General calculation parameters included a 20 Hartree electronic energy cutoff, spin polarization, no symmetry constraints, a Γ-centered k-point grid with a density of  $1000/N_{atoms}$ , and an energy convergence threshold of 1 meV. Calculations of surfaces and adsorbate systems were performed using the CANDLE linear PCM solvation model for H<sub>2</sub>O, with 0.5 M Na<sup>+</sup> and F<sup>-</sup> ions.  $^{28,43}$  A more complete description of the methods used to calculate and generate reaction pathways (Figure 2) is provided in Section S1.

All reaction pathways were shifted so that the final state,  $2NH_3$  or  $H_2$ , was defined as having a grand free energy of 0 eV. This shifts the initial state,  $N_2$  and six protons for NRR, two protons for HER, as the bias becomes more reducing due to the relative destabilization (stabilization) of protons (electrons) in the solvent (bulk electrode). This represents the system more accurately than setting the initial state of the reaction pathway as the reference, which implies that the neutral product molecules  $NH_3$  and  $H_2$  are stabilized by a

more reducing bias. Additional discussion of reference states is available in Section S1.

Orbital projected density of states (pDOS) were calculated for specific surface and adsorbate systems using JDFTx. Calculated pDOS were plotted with the Gaussian smearing of 0.1 eV using Pymatgen<sup>44</sup> and centered to the Fermi level.

Grand Canonical Nudged Elastic Band Approach. We implemented the GC-NEB approach to calculate TS pathways as a function of bias while allowing the fractional transfer of electrons between the surface and adsorbate throughout the TS pathway. GC-NEB is only the second implementation of a fully grand-canonical approach for relaxing TS pathways in equilibrium with an applied bias. 45 We improved the base JDFTx calculator in the pythonic atomic simulation environment (ASE),<sup>46</sup> to enable its use with the ASE implementation of the NEB method. 47,48 This allowed each NEB image to be calculated with JDFTx at the corresponding bias with an independent charge density and solvent response. GC-NEB calculation parameters are readily switched between a variety of different solvent models, biases, NEB optimizers, TS images, DFT functionals, etc., and this code can be readily applied to any surface and adsorbate calculations. The GC-NEB code is available at https://github.com/Nick-Singstock/GC-NEB and contains a detailed description and tutorials to set up and run GC-DFT and GC-NEB calculations.

In this work, we used five NEB images (not including the initial and final states) to calculate the TS pathways and  $\Phi_a\cdot\Phi_a$  is calculated as the difference between the maximum energy along the converged TS path and the energy of the initial state. For protonation reactions, an  $H_3O^+$  molecule was placed above the atom being protonated, with a hydrogen atom pointing in the z-direction toward the surface, separated from the atom being protonated by 1.8 Å. The final state included both the protonated adsorbate and the remaining  $H_2O$  molecule above the surface.

**Microkinetic Model.** A microkinetic model was developed that includes NRR and HER steps to calculate the coverage of different adsorbates, the reaction rates of the elementary steps, the current density for NRR and HER, the mass yield of  $NH_3$  and  $H_2$ , and the FE of NRR. Detailed descriptions of the calculations of elementary step rate constants, steady-state adsorbate coverages, and microkinetic model outputs are included in Section S3.

# ASSOCIATED CONTENT

# Supporting Information

The Supporting Information is available free of charge at https://pubs.acs.org/doi/10.1021/jacs.2c03661.

Calculation details, microkinetic model parameters, and additional figures for dissociative  $N_2$  dissociation, adsorption at sulfur sites, NRR activity and selectivity diagrams, and reaction energetics (PDF)

# AUTHOR INFORMATION

# **Corresponding Author**

Charles B. Musgrave — Department of Chemical and Biological Engineering, University of Colorado Boulder, Boulder, Colorado 80303, United States; Materials Science and Engineering Program and Renewable and Sustainable Energy Institute, University of Colorado Boulder, Boulder, Colorado 80303, United States; orcid.org/0000-0002-5732-3180; Email: charles.musgrave@colorado.edu

#### **Author**

Nicholas R. Singstock — Department of Chemical and Biological Engineering, University of Colorado Boulder, Boulder, Colorado 80303, United States; Occid.org/0000-0003-2093-0216

Complete contact information is available at: https://pubs.acs.org/10.1021/jacs.2c03661

### **Author Contributions**

N.R.S. and C.B.M. contributed equally to this manuscript.

The authors declare no competing financial interest.

## ACKNOWLEDGMENTS

NRS was supported by the National Science Foundation (awards CBET-1806079 and CBET-2016225). NRS and CBM also acknowledge support from the U.S. Department of Energy, Office of Science, Basic Energy Sciences (DE-SC0022247). This work utilized resources from the University of Colorado Boulder Research Computing Group, which is supported by the National Science Foundation (awards ACI-1532235 and ACI-1532236), the University of Colorado Boulder, and Colorado State University.

# ABBREVIATIONS

NRR nitrogen reduction reaction HER hydrogen evolution reaction

FE Faradaic efficiency

GC-DFT grand-canonical density functional theory GC-NEB grand-canonical nudged elastic band method

RDS rate-determining step
TS transition state

CHE computational hydrogen electrode method

# REFERENCES

- (1) Erisman, J. W.; Sutton, M. A.; Galloway, J.; Klimont, Z.; Winiwarter, W. How a Century of Ammonia Synthesis Changed the World. *Nat. Geosci.* **2008**, *1*, 636–639.
- (2) Chen, J. G.; Crooks, R. M.; Seefeldt, L. C.; Bren, K. L.; Morris Bullock, R.; Darensbourg, M. Y.; Holland, P. L.; Hoffman, B.; Janik, M. J.; Jones, A. K.; et al. Beyond Fossil Fuel—Driven Nitrogen Transformations. *Science* **2018**, *360*, No. eaar6611.
- (3) Han, G. F.; Li, F.; Chen, Z. W.; Coppex, C.; Kim, S. J.; Noh, H. J.; Fu, Z.; Lu, Y.; Singh, C. V.; Siahrostami, S.; et al. Mechanochemistry for Ammonia Synthesis under Mild Conditions. *Nat. Nanotechnol.* **2021**, *16*, 325–330.
- (4) Guo, C.; Ran, J.; Vasileff, A.; Qiao, S. Rational Design of Electrocatalysts and Photo(Electro)Catalysts for Nitrogen Reduction to Ammonia (NH3) under Ambient Conditions. *Energy Environ. Sci.* **2018**, *11*, 45–56.
- (5) Humphreys, J.; Lan, R.; Tao, S. Development and Recent Progress on Ammonia Synthesis Catalysts for Haber–Bosch Process. *Adv. Energy Sustainability Res.* **2021**, *2*, No. 2000043.
- (6) Cao, N.; Zheng, G. Aqueous Electrocatalytic N2 Reduction under Ambient Conditions. *Nano Res.* **2018**, *11*, 2992–3008.
- (7) Lim, J.; Fernández, C. A.; Lee, S. W.; Hatzell, M. C. Ammonia and Nitric Acid Demands for Fertilizer Use in 2050. *ACS Energy Lett.* **2021**, *6*, 3676–3685.
- (8) Wang, L.; Xia, M.; Wang, H.; Huang, K.; Qian, C.; Maravelias, C. T.; Ozin, G. A. Greening Ammonia toward the Solar Ammonia Refinery. *Joule* **2018**, *2*, 1055–1074.
- (9) David, B.; Bird, F.; Clarke, A.; Davies, P.; Surkovic, E. Ammonia: Zero-Carbon Fertiliser, Fuel and Energy Store; 2020.
- (10) Suryanto, B. H. R.; Du, H.-L.; Wang, D.; Chen, J.; Simonov, A.; MacFarlane, D. Challenges and Prospects in the Catalysis of

- Electroreduction of Nitrogen to Ammonia. Nat. Catal. 2019, 2, 290–296.
- (11) Tang, C.; Qiao, S. Z. How to Explore Ambient Electrocatalytic Nitrogen Reduction Reliably and Insightfully. *Chem. Soc. Rev.* **2019**, 48, 3166–3180.
- (12) Service, R. F. Liquid Sunshine. Science 2018, 361, 120-123.
- (13) Zhao, X.; Hu, G.; Chen, G. F.; Zhang, H.; Zhang, S.; Wang, H. Comprehensive Understanding of the Thriving Ambient Electrochemical Nitrogen Reduction Reaction. *Adv. Mater.* **2021**, 33, No. 2007650.
- (14) Andersen, S. Z.; Čolić, V.; Yang, S.; Schwalbe, J. A.; Nielander, A. C.; McEnaney, J. M.; Enemark-Rasmussen, K.; Baker, J. G.; Singh, A. R.; Rohr, B. A.; et al. A Rigorous Electrochemical Ammonia Synthesis Protocol with Quantitative Isotope Measurements. *Nature* **2019**, *570*, 504–508.
- (15) Li, W.; Li, K.; Ye, Y.; Zhang, S.; Liu, Y.; Wang, G.; Liang, C.; Zhang, H.; Zhao, H. Efficient Electrocatalytic Nitrogen Reduction to Ammonia with Aqueous Silver Nanodots. *Commun. Chem.* **2021**, *4*, No. 10.
- (16) Xu, H.; Ithisuphalap, K.; Li, Y.; Mukherjee, S.; Lattimer, J.; Soloveichik, G.; Wu, G. Electrochemical Ammonia Synthesis through N2 and H2O under Ambient Conditions: Theory, Practices, and Challenges for Catalysts and Electrolytes. *Nano Energy* **2020**, *69*, No. 104469.
- (17) Foster, S. L.; Bakovic, S. I. P.; Duda, R. D.; Maheshwari, S.; Milton, R. D.; Minteer, S. D.; Janik, M. J.; Renner, J. N.; Greenlee, L. F. Catalysts for Nitrogen Reduction to Ammonia. *Nat. Catal.* **2018**, *1*, 490–500
- (18) Zhang, L.; Ji, X.; Ren, X.; Ma, Y.; Shi, X.; Tian, Z.; Asiri, A. M.; Chen, L.; Tang, B.; Sun, X.; et al. Electrochemical Ammonia Synthesis via Nitrogen Reduction Reaction on a MoS2 Catalyst: Theoretical and Experimental Studies. *Adv. Mater.* **2018**, *30*, No. 1800191.
- (19) Jin, H.; Li, L.; Liu, X.; Tang, C.; Xu, W.; Chen, S.; Song, L.; Zheng, Y.; Qiao, S.-Z.; Jin, H.; et al. Nitrogen Vacancies on 2D Layered W2N3: A Stable and Efficient Active Site for Nitrogen Reduction Reaction. *Adv. Mater.* **2019**, *31*, No. 1902709.
- (20) Song, Y.; Johnson, D.; Peng, R.; Hensley, D. K.; Bonnesen, P. V.; Liang, L.; Huang, J.; Yang, F.; Zhang, F.; Qiao, R.; et al. A Physical Catalyst for the Electrolysis of Nitrogen to Ammonia. *Sci. Adv.* **2018**, *4*, No. e1700336.
- (21) Montoya, J. H.; Tsai, C.; Vojvodic, A.; Nørskov, J. K. The Challenge of Electrochemical Ammonia Synthesis: A New Perspective on the Role of Nitrogen Scaling Relations. *ChemSusChem* **2015**, *8*, 2180–2186.
- (22) Sippel, D.; Rohde, M.; Netzer, J.; Trncik, C.; Gies, J.; Grunau, K.; Djurdjevic, I.; Decamps, L.; Andrade, S. L. A.; Einsle, O. A Bound Reaction Intermediate Sheds Light on the Mechanism of Nitrogenase. *Science* **2018**, 359, 1484–1489.
- (23) Čorić, I.; Mercado, B. Q.; Bill, E.; Vinyard, D. J.; Holland, P. L. Binding of Dinitrogen to an Iron—Sulfur—Carbon Site. *Nature* **2015**, 526, 96—99.
- (24) Lukoyanov, D. A.; Yang, Z.-Y.; Dean, D. R.; Seefeldt, L. C.; Raugei, S.; Hoffman, B. M. Electron Redistribution within the Nitrogenase Active Site FeMo-Cofactor During Reductive Elimination of H2 to Achieve N≡N Triple-Bond Activation. *J. Am. Chem. Soc.* 2020, 142, 21679−21690.
- (25) Lu, K.; Xia, F.; Li, B.; Liu, Y.; Razak, I. B. A.; Gao, S.; Kaelin, J.; Brown, D. E.; Cheng, Y. Synergistic Multisites Fe2Mo6S8 Electrocatalysts for Ambient Nitrogen Conversion to Ammonia. *ACS Nano* **2021**, *15*, 16887–16895.
- (26) Akbashev, A. R. Electrocatalysis Goes Nuts. ACS Catal. 2022, 12, 4296–4301.
- (27) Resasco, J.; Abild-Pedersen, F.; Hahn, C.; Bao, Z.; Koper, M. T. M.; Jaramillo, T. F. Enhancing the Connection between Computation and Experiments in Electrocatalysis. *Nat. Catal.* **2022**, *5*, 374–381.
- (28) Schwarz, K.; Sundararaman, R. The Electrochemical Interface in First-Principles Calculations. *Surf. Sci. Rep.* **2020**, *75*, No. 100492.
- (29) Alsunni, Y. A.; Alherz, A. W.; Musgrave, C. B. Electrocatalytic Reduction of CO2 to CO over Ag(110) and Cu(211) Modeled by

- Grand-Canonical Density Functional Theory. J. Phys. Chem. C 2021, 125, 23773-23783.
- (30) Liu, C.; Qian, J.; Ye, Y.; Zhou, H.; Sun, C. J.; Sheehan, C.; Zhang, Z.; Wan, G.; Liu, Y. S.; Guo, J.; et al. Oxygen Evolution Reaction over Catalytic Single-Site Co in a Well-Defined Brookite TiO2 Nanorod Surface. Nat. Catal. 2021, 4, 36-45.
- (31) Varley, J. B.; Wang, Y.; Chan, K.; Studt, F.; Nørskov, J. K. Mechanistic Insights into Nitrogen Fixation by Nitrogenase Enzymes. Phys. Chem. Chem. Phys. 2015, 17, 29541-29547.
- (32) Hoffman, B. M.; Lukoyanov, D.; Yang, Z. Y.; Dean, D. R.; Seefeldt, L. C. Mechanism of Nitrogen Fixation by Nitrogenase: The next Stage. Chem. Rev. 2014, 114, 4041-4062.
- (33) Lilova, K.; Perryman, J. T.; Singstock, N. R.; Abramchuk, M.; Subramani, T.; Lam, A.; Yoo, R.; Ortiz-Rodríguez, J. C.; Musgrave, C. B.; Navrotsky, A.; Velázquez, J. M. A Synergistic Approach to Unraveling the Thermodynamic Stability of Binary and Ternary Chevrel Phase Sulfides. Chem. Mater. 2020, 32, 7044-7051.
- (34) Spivey, T. D.; Holewinski, A. Selective Interactions between Free-Atom-like d-States in Single-Atom Alloy Catalysts and Near-Frontier Molecular Orbitals. J. Am. Chem. Soc. 2021, 143, 11897-
- (35) Perryman, J. T.; Hyler, F. P.; Ortiz-Rodríguez, J. C.; Mehta, A.; Kulkarni, A. R.; Velázquez, J. M. X-Ray Absorption Spectroscopy Study of the Electronic Structure and Local Coordination of 1st Row Transition Metal-Promoted Chevrel-Phase Sulfides. J. Coord. Chem. 2019, 72, 1322-1335.
- (36) Singstock, N. R.; Ortiz-Rodríguez, J. C.; Perryman, J. T.; Sutton, C.; Velázquez, J. M.; Musgrave, C. B. Machine Learning Guided Synthesis of Multinary Chevrel Phase Chalcogenides. J. Am. Chem. Soc. 2021, 143, 9113-9122.
- (37) Ortiz-Rodríguez, J. C.; Singstock, N. R.; Perryman, J. T.; Hyler, F. P.; Jones, S. J.; Holder, A. M.; Musgrave, C. B.; Velázquez, J. M. Stabilizing Hydrogen Adsorption through Theory-Guided Chalcogen Substitution in Chevrel-Phase Mo6X8 (X = S, Se, Te) Electrocatalysts. ACS Appl. Mater. Interfaces 2020, 12, 35995-36003.
- (38) Perryman, J. T.; Velázquez, J. M. Design Principles for Multinary Metal Chalcogenides: Toward Programmable Reactivity in Energy Conversion. Chem. Mater. 2021, 33, 7133-7147.
- (39) Sundararaman, R.; Letchworth-Weaver, K.; Schwarz, K. A.; Gunceler, D.; Ozhabes, Y.; Arias, T. A. JDFTx: Software for Joint Density-Functional Theory. SoftwareX 2017, 6, 278-284.
- (40) Sundararaman, R.; Goddard, W. A.; Arias, T. A. Grand Canonical Electronic Density-Functional Theory: Algorithms and Applications to Electrochemistry. J. Chem. Phys. 2017, 146, No. 114104.
- (41) Perdew, J. P.; Burke, K.; Ernzerhof, M. Generalized Gradient Approximation Made Simple. Phys. Rev. Lett. 1996, 77, 3865-3868.
- (42) Grimme, S. Semiempirical GGA-Type Density Functional Constructed with a Long-Range Dispersion Correction. J. Comput. Chem. 2006, 27, 1787-1799.
- (43) Sundararaman, R.; Goddard, W. A. The Charge-Asymmetric Nonlocally Determined Local-Electric (CANDLE) Solvation Model. J. Chem. Phys. 2015, 142, No. 064107.
- (44) Ong, S. P.; Richards, W. D.; Jain, A.; Hautier, G.; Kocher, M.; Cholia, S.; Gunter, D.; Chevrier, V. L.; Persson, K. A.; Ceder, G. Python Materials Genomics (Pymatgen): A Robust, Open-Source Python Library for Materials Analysis. Comput. Mater. Sci. 2013, 68,
- (45) Kastlunger, G.; Lindgren, P.; Peterson, A. A. Controlled-Potential Simulation of Elementary Electrochemical Reactions: Proton Discharge on Metal Surfaces. J. Phys. Chem. C 2018, 122, 12771-12781.
- (46) Larsen, A. H.; Mortensen, J. J.; Blomqvist, J.; Castelli, I. E.; Christensen, R.; Dułak, M.; Friis, J.; Groves, M. N.; Hammer, B.; Hargus, C.; et al. The Atomic Simulation Environment-a Python Library for Working with Atoms. J. Phys. Condens. Matter 2017, 29, No. 273002.

(47) Mills, G.; Jónsson, H. Quantum and Thermal Effects in H2 Dissociative Adsorption: Evaluation of Free Energy Barriers in Multidimensional Quantum Systems. Phys. Rev. Lett. 1994, 72, 1124. (48) Henkelman, G.; Uberuaga, B. P.; Jónsson, H. A Climbing Image Nudged Elastic Band Method for Finding Saddle Points and Minimum Energy Paths. J. Chem. Phys. 2000, 113, 9901.

# **□** Recommended by ACS

The Influence of Single-Atom Fe2+/3+N4 Spin State on the Electroreduction of CO2 to CO/HCOOH by Analyzing Proton/Electron Transfer Mechanisms an...

Yuxin Xie, Xiaohua Chen, et al.

SEPTEMBER 24, 2021

THE JOURNAL OF PHYSICAL CHEMISTRY C

Phosphorus-Driven Electron Delocalization on Edge-Type FeN4 Active Sites for Oxygen Reduction in Acid Medium

Hengbo Yin, Jia-Nan Zhang, et al.

OCTOBER 05, 2021

ACS CATALYSIS

READ

**Probing the Oxygen Reduction Reaction Intermediates** and Dynamic Active Site Structures of Molecular and Pyrolyzed Fe-N-C Electrocatalysts by In Situ Raman...

Jie Wei, Lin Gan, et al.

JUNE 16, 2022

ACS CATALYSIS

READ **C** 

Two Types of Single-Atom FeN4 and FeN5 **Electrocatalytic Active Centers on N-Doped Carbon** Driving High Performance of the SA-Fe-NC Oxygen ...

Xiao Liang, Lirong Zheng, et al.

JULY 16, 2021

CHEMISTRY OF MATERIALS

READ 2

Get More Suggestions >